Mesostructural analysis of micron-sized glass particles during shear deformation – a direct comparison of experiment and simulation

L. Handl[a,*], L. Torbahn[b], A. Weuster[c], A. Spettl[a], L. Brendel[c], D. E. Wolf[c], V. Schmidt[a], A. Kwade[b]

[a] *Insitute of Stochastics, Universität Ulm, Helmholtzstr. 18, 89069 Ulm, Germany*
[b] *Institute for Particle Technology (iPAT), Technische Universität Braunschweig, Volkmaroder Str. 5, 38104 Braunschweig, Germany*
[c] *Center for Nanointegration Duisburg-Essen (CeNIDE) and Universität Duisburg-Essen, Lotharstr. 1, 47057 Duisburg, Germany*

Abstract

The interplay between structure and mechanical properties of fine and cohesive granular matter is of wide interest and far from being well understood. Even though the discrete element method (DEM) supplies a powerful and extensively applied tool for modeling granular matter, the complexity in contact mechanics of micron-sized particles demands a complex contact model. In order to validate DEM simulations, a direct comparison to experiments is desirable. However, the simulation of a full-scale shear-tester with micron-sized particles remains a great challenge. We address this validation problem by scaling the experiment down: For this purpose, a fully functional micro shear-tester was developed and implemented into an X-ray tomography device (XMT). This combination allows the visualization of all particles within small bulk volumes of the order of a few µl under well-defined consolidation conditions. Using spherical micron-sized particles (~ 30 µm), torsional shear tests with a number of particles which is practicable for simulations can be performed. Moreover, an analysis on particle level allows for a direct comparison of the structural evolution to numerical results. In this study, we present methods to localize and track particles in the experimental 3D image data. This is possible even for large angle increments of up to 5° between tomographic measurements. The processing of time-resolved tomographic data makes it possible to analyze the behavior of particles, which is then compared to DEM simulations of a similar experiment. We focus on density inhomogeneity and shear induced heterogeneity and observe very good agreement of shear band location and shape in the steady state.

Keywords: shear flow, glass beads, micro shear-tester, DEM simulations, particle tracking, shear band

1. Introduction

Shear flow of granular media is ubiquitous in nature and of industrial importance when it comes to handling and processing of bulk solids (e.g., flow through hoppers [1], bunkers and silos [2, 3]). In the physics of granular matter [4], among many other interesting phenomena, understanding the flow properties, i.e., the stress response to an applied strain rate, has been in the focus of research [5]. In addition, a strain rate independent creep regime arises at slow, quasi-static deformation [6, 7]. The localization of strain within the bulk, often referred to as failure zone or shear band, represents another unique feature of this quasi-static regime, which was addressed by many researchers in the past [8, 9, 10, 11] and can be observed, e.g., in glassy systems [12] and solidifying metals [13] as well. However, the interplay of structure and mechanical properties of the bulk solid is not deciphered sufficiently, especially when it comes to cohesive granular matter.

Modern technology offers a variety of powerful tools to pursue this task: On the one hand, numerical simulations in terms of the discrete element method (DEM) provide valuable insight into the mechanical behavior of granular matter [14, 15, 16], and allow to study the influence of microscopic contact and particle properties on the macroscopic bulk behavior systematically [17, 18]. However, despite of Moore's law, the simulation of full-scale quasi-static shear experiments with realistic particle interactions remains a challenge. Since scaling of particle size can be problematic [19], most numerical studies are limited to a small sample size. On the other hand, sophisticated experimental setups are capable of determining the properties of micron-sized particles [20] and of imaging the inner structure of a bulk solid nondestructively via computer tomography [21, 22]. Using this methodology, we explore the potential of DEM simulations and micro-sized experiments by performing a direct comparison. For this task, a fully functional micro-sized shear tester was developed [21], which can be fitted into an X-ray tomography device. As will be shown, this setup allows an in-situ shear band detection during an experiment at constant normal load with only a few µl of sample volume. Other experiments which explore the inner structure of a bulk solid do not focus on a constant normal load (e.g. using confocal-microscopy [23]), or use simply a flexible tube to execute a triaxial-like shear experiment [24]. Besides the promising possibility to examine the structure of the bulk solid at mesoscale, the micro shear-tester is also well suited for determining shear flow properties of powders which are only available in small quantities.

*Corresponding author. Tel: +49 731/50-23528; Fax: +49 731/50-23649
Email address: lisa.handl@uni-ulm.de (L. Handl)

With regard to DEM simulations, this micro-sized experiment offers a unique chance of an increased validation depth via a direct comparison of the bulk structure and its dynamics. Describing the contact mechanics of micron-sized particles correctly is often accompanied by a cumbersome amount of parameters which are not easily accessed in the experiment. Therefore, a conventional approach is to calibrate undetermined parameters, which may also compensate other idealizations [25]. Sometimes even guessing parameters seems reasonable, but a desirable objective would be a simple model without superfluous parameters, which describes the system of interest and can be utilized for quantitatively correct predictions. To which extent simple contact models can predict the bulk's inner structure correctly will be explored within this study.

The paper is structured as follows: Sections 2.1 and 2.2 are devoted to the experimental setup as well as the model material. The methodology of image segmentation and particle tracking is described in Section 2.3, while the numerical calculations including the contact model and simulation setup are explained in Section 2.4. Results will be presented in Section 3 and discussed in Section 4.

2. Material and methods

2.1. Material

In this study we use a fine and slightly cohesive powder which consists of solid borosilicate glass microspheres (BSGMS 27-32 µm, CoSpheric LLC, USA; BSGMS in the following). An image of several microsphere particles taken on a scanning electron microscope (SEM) is presented in Figure 1 (inset). The figure emphasizes the almost uniform spherical shape and similar size of the particles, but also shows a non-negligible surface roughness. We measured the particle size distribution using laser diffraction (Helos, Sympatec GmbH, Germany) after dispersing the particles with ultrasound for 30 s in an aqueous environment. The results, which are shown in Figure 1, indicate a narrow mono-disperse size distribution of the glass particles with median value $x_{50,3} \approx 30$ µm.

Particle stiffness and adhesion forces were determined in [26] using nanoindentation and atomic force microscopy, respectively. The reported mean values and standard deviations are $E \approx 15 \pm 7$ GPa for the elastic modulus and 82 nN ± 60 nN for adhesion forces.

2.2. Experiment

2.2.1. X-ray microtomography (XMT)

The fundamental component for a detailed microstructural investigation is the nondestructive examination with the XMT, which enables an image-based analysis. We use a high-resolution tomography device (MicroXCT-400, Zeiss (Xradia), Germany). For this study an acceleration voltage of 50 kV and a current intensity of 200 µA were applied at the X-ray source. These parameters result in the best outcome for high-contrast images. According to the sample diameter of 2 mm a ten-fold optical magnification is used to ensure a reproduction of the entire sample diameter with a resolution of 2.2 µm (1.1 µm before binning). A single detector collected the X-rays which were emitted from the source and passed through the sample which results in an intensity grayscale image. In order to get an accurate 3D reconstruction afterwards, we measured 2000 of these projections for various angles of rotation around an axis inside the sample. The reconstructed data is stored in stacks of 2D images for later analysis with regard to structure and dynamics. Depending on the device resolution and the particle size, investigations on mesoscale as well as on particle scale are possible. Thus, the detailed data on particle scale qualifies for finding relations between particle parameters (e.g., size, shape and aspect ratio) and mesoscale or bulk behavior (e.g., shear zone characteristics).

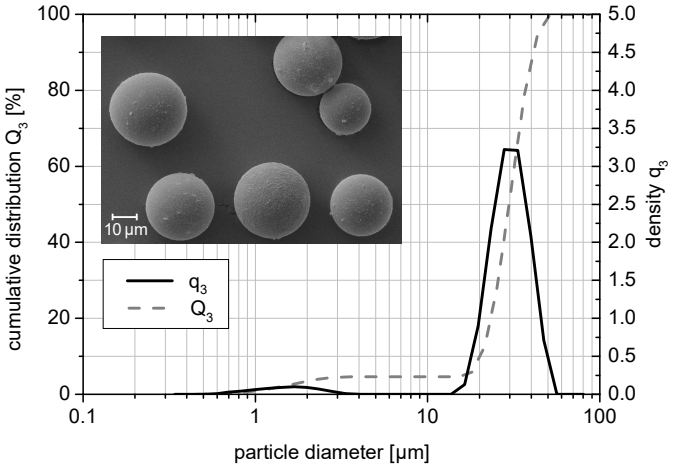

Figure 1: Particle size distribution (mass distribution, density and cumulative distribution function) and SEM picture (inset) of BSGMS glass particles.

2.2.2. Micro shear-tester

The torsional micro shear-tester with cylindrical shear cell was developed to handle very small sample volumes in the range of 6-15 µl [26]. In combination with the XMT, the samples can easily be manipulated in terms of compression and shear deformation on the one hand, and imaged in 3D at a very high resolution on the other hand. A cylindrical sample chamber with a radius of $R = 1$ mm allows for an (in principle) infinite torsional shear movement. The sample chamber is a very fine borosilicate glass capillary with a side wall thickness of 50 µm and is confined by an upper and lower piston in vertical direction. The pistons can be flat for simple compression tests or structured with six vanes arranged in a regular star shape for shear tests like presented in this work. A schematic image of the shear cell can be found in Figure 2. During shear, the upper piston and outer wall move whereas the lower piston detects the normal force and torque. For vertical force transmission a magnetic spring was included at the lower piston as well as a frictionless air suspension to prevent or at least minimize friction. A major advantage of this system is the decoupled determination of force and torque. Loads in the range of 0.1-20 kPa can be applied by the micro shear-tester.

The sample is prepared by sieving the particles into the glass capillary in order to avoid agglomeration. The normal load is

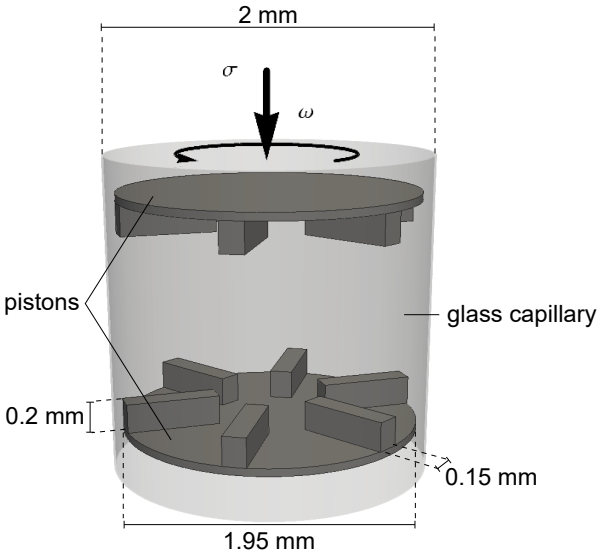

Figure 2: Schematic view of the shear cell of the micro shear-tester.

increased up to 0.5 kPa and kept constant in the following shear process. During shear, the upper piston and wall are rotated in steps of 0.5° up to 9.5°. After 9.5° the angle increment is increased to 5° until an entire rotation of 39.5° is achieved. The experiment is carried out quasi-statically with an angular velocity of $\omega = 0.1$ °/s. Directly after compaction and after each step of shearing an XMT measurement of the entire shear cell is recorded. The resulting 3D image stacks are aligned and cut to the size of the sample chamber, so that they have the same dimension in x- and y-direction but different sizes in z-direction (depending on dilation/compaction during shear). The maximum z-coordinate of the image stack recorded at time t is denoted by $z^t_{\max}$, where t is the time of shearing — i.e., we neglect the pauses necessary for XMT measurements.

2.3. Analysis

2.3.1. Image-based local shear deformation

A first approximation of the local shear deformation is computed directly from the image data in a similar way as proposed in [26]. The idea of this approach is to compare the image slices at two successive points in time and a fixed height z. The local shear angle at height z is the angle by which the first slice has to be rotated so that it best matches the second slice. This approach relies on a strong similarity between the particle structures at two consecutive points in time. Thus, it requires a sufficiently high spatial and temporal resolution.

The quality criterion used in this study to determine how closely the two slices match is the image cross-correlation,

$$\mathrm{corr}(I, J) = \frac{\sum_{x,y}(I(x,y) - \bar{I})(J(x,y) - \bar{J})}{\sigma_I \cdot \sigma_J}, \qquad (1)$$

where $I = \{I(x,y)\}$ and $J = \{J(x,y)\}$ are digital 2D images, $\bar{I}$ and $\bar{J}$ are the mean values, and σ_I and σ_J are the standard deviations of gray values taken over all pixels in I and J, respectively. For a time step (t_1, t_2) the local angle of shear deformation at height z is estimated by computing

$$\Delta_\varphi^{t_1 \to t_2}(z) = \underset{\alpha \in [-1°,\ \Delta\varphi_s(t_1,t_2)+1°]}{\arg\max} \left\{ \mathrm{corr}\left(\mathrm{rot}_\alpha(I^z_{t_1}), I^z_{t_2} \right) \right\}, \qquad (2)$$

where I^z_t denotes the slice at height z and time t, rot_α denotes the rotation around the image center by the angle α, and $\Delta\varphi_s(t_1, t_2)$ is the angle increment used in time step (t_1, t_2). Theoretically, optimization over the full range $\alpha \in [0, 360)$ would be desirable. For computational reasons we restrict it to a realistic range in Equation (2). The image rotations are carried out using bilinear interpolation and the maximization is implemented in discrete steps of 0.1°. Applying the same procedure for all available z-coordinates yields a spatially resolved local shear deformation over the full height of the sample.

The same methodology can be used to measure the rotation of the upper and lower piston in the image data. This is necessary because there may be differences between the targeted and actual movements of the pistons, which will be discussed in more detail later (cf. Section 3.2). We simply average $\Delta_\varphi^{t_1 \to t_2}(z)$ over the range of z-coordinates in which the upper and lower piston, respectively, are visible. Since an exact measurement of these movements is crucial for a correct normalization of particle velocities later on (and less computationally expensive than estimating $\Delta_\varphi^{t_1 \to t_2}(z)$ over the full height of the sample), optimization is carried out in steps of 0.01°.

The idea of estimating shear deformation locally from the image data can be extended further to capture radial variations of the local deformation and to estimate local compression or dilation along with the rotational deformation. For this purpose, each image slice is subdivided into k disjoint and concentric rings of equal area, $R_1, \ldots, R_k$, and a rotational *and* translational deformation are applied simultaneously. This means that instead of rotating the image slice as a whole, each ring is rotated independently and shifted vertically so that it best matches the corresponding region of the next image stack. We then obtain the 2D maximization problem

$$\left(\Delta_\varphi^{t_1 \to t_2}(z, r_i),\ \Delta_z^{t_1 \to t_2}(z, r_i)\right) = \underset{\substack{h \in [h_{\min}, \ldots, h_{\max}] \\ \alpha \in [-1°,\ \Delta\varphi_s(t_1,t_2)+1°]}}{\arg\max} \left\{ \mathrm{corr}\left(\mathrm{rot}_\alpha(I^{z,R_i}_{t_1}), I^{z+h,R_i}_{t_2} \right) \right\}, \qquad (3)$$

where r_i is the central radius of R_i, I^{z,R_i}_t denotes the ring R_i of the image slice at height z and time t, and $i \in \{1, \ldots, k\}$. The result is a local angle of shear and a local vertical deformation for each z-coordinate and ring, R_i. Using bilinear interpolation we can calculate values for the deformation at arbitrary locations in the sample. In this study $k = 10$ rings are used and the range for the vertical shift is chosen based on the stack sizes in z-direction, $z^{t_1}_{\max}$ and $z^{t_2}_{\max}$, as

$$[h_{\min}, \ldots, h_{\max}] = \left[\min\{z^{t_2}_{\max} - z^{t_1}_{\max}, 0\}, \ldots, \max\{z^{t_2}_{\max} - z^{t_1}_{\max}, 0\} \right].$$

In the following, we will refer to the left-hand sides of Equations (2) and (3) as 1D and 2D image-based local shear deformation, respectively. Both methods are applied and discussed in this paper.

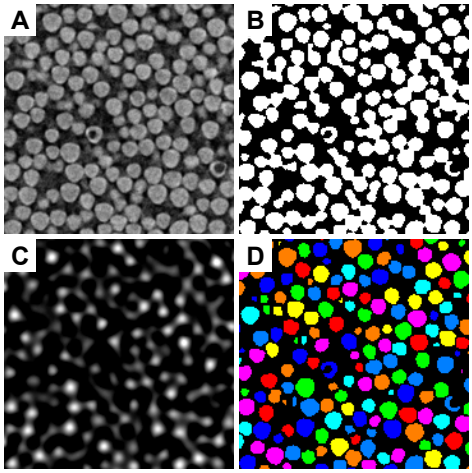

Figure 3: Visualization of the main steps of the segmentation process based on a small cutout of an image slice. Grayscale image obtained by XMT (A), binary image (B), convolution of grayscale image and particle mask used for marker selection (C) and final segmentation result after applying the marker-based watershed transform (D). Note that though the visualization is in 2D, all operations are carried out in 3D.

2.3.2. *Image segmentation*

In order to extract information on single particles from the image data, 3D images are segmented using a marker-based watershed transformation [27]. First, the grayscale images are smoothed using a Gaussian filter with a small standard deviation of 1 voxel side length, and binarized using the IsoData algorithm implemented in ImageJ [28]. Subsequently, small disconnected pores are filled with solid. This step is needed because a small percentage of the particles is hollow. The negative of the Euclidean distance transform (distances from particle voxels to the pore phase) forms the relief on which the watershed transformation is run.

A common choice for the markers is to select the local maxima of the Euclidean distance transform [27]. However, this choice tends to promote over-segmentation since minor surface roughnesses can lead to multiple local maxima within one particle. In the present study this problem is avoided by using an approach presented in [23], where the original grayscale images are convolved with a mask resembling the appearance of a particle. After convolution, the particle centers appear as smooth and isolated local intensity maxima. These maxima are extracted from the convolved images and used as markers for the watershed transformation. The convolution technique is ideal for spherical particles with a narrow size distribution as used in this study, although it can be adapted for broader size distributions as shown in [23]. The main steps of the segmentation process are visualized in Figure 3.

2.3.3. *Particle tracking*

Based on the centers of mass of the particles in the segmented binary images, a particle tracking is performed. The tracking algorithm used in this study for time steps with an angle increment of 0.5° has been proposed in [29] and aims to minimize the sum of squared displacements in each time step. For computational reasons the optimization is not carried out directly in [29], but on a reduced problem. Assignments between particles of two consecutive points in time are discarded if the distance between the particles exceeds a certain threshold, s. This simplification typically leads to a decomposition of the optimization problem into a number of smaller problems, which can be solved independently and much faster. The threshold value has been set to $s = 19.8$ µm in the current study.

Minimizing the sum of squared displacements is feasible as long as very little movement occurs within a time step. In particular, particle movements in one step have to be less than the threshold value, s. This is most likely true for shearing steps of 0.5° since a particle will be displaced by at most 8.72 µm theoretically (arc length at the upper, outer edge of the cylinder). However, when shearing in steps of 5°, particle displacements of ten times the size, i.e., of up to 87.2 µm, have to be expected. In this case a tracking computed by minimizing displacements will clearly be wrong and it is impossible to obtain satisfying results without prior information on the dynamics in the particle system.

The 2D image-based local shear deformation (cf. Section 2.3.1) essentially describes the average movement of particles depending on their location in the sample — and this is used as prior information for tracking particles in steps with an angle increment of 5°. For every particle at time t_1, a hypothetical position for where it is expected to be at time t_2 is calculated based on the 2D image-based local shear deformation, $(\Delta_\varphi^{t_1\to t_2}, \Delta_z^{t_1\to t_2})$. This is done by rotating each particle center (r_p, φ_p, z_p) around the central axis of the cylinder by the angle $\Delta_\varphi^{t_1\to t_2}(z_p, r_p)$ and shifting it vertically by $\Delta_z^{t_1\to t_2}(z_p, r_p)$. Then, the sum of squared distances between the hypothetical and actual particle positions at time t_2 is minimized, where now all assignments leading to a larger distance between hypothetical and actual position than some threshold, $\tilde{s}$, are discarded. Here we obtained good results for $\tilde{s} = 17.6$ µm.

This approach for tracking in steps of 1° or more is validated using the data from 3.5° to 9.5° of shearing, which is available in steps of 0.5° and where no more major compression occurs. For this whole period, a particle tracking has been computed based on all available data and the original method described in [29]. This will be referred to as reference tracking in the following. In order to validate the tracking method based on the local shear deformation, it has been applied to each of the intervals from 3.5° to 4°, from 3.5° to 4.5°, ..., and from 3.5° to 9.5° of shearing, taking into account only the first and last point in time, respectively. In particular, no information on intermediate time steps is used. The resulting tracks have been compared to the ground truth, i.e., each track is considered correct if its starting and end point belong to the same track in the reference tracking. The fraction of correct tracks decreases slowly with increasing angle increment. For an angle increment of 5° (or smaller) more than 98.5 % of the computed tracks agree with the reference tracking. Even with an angle increment of 6°, more than 98 % of the tracks are correct.

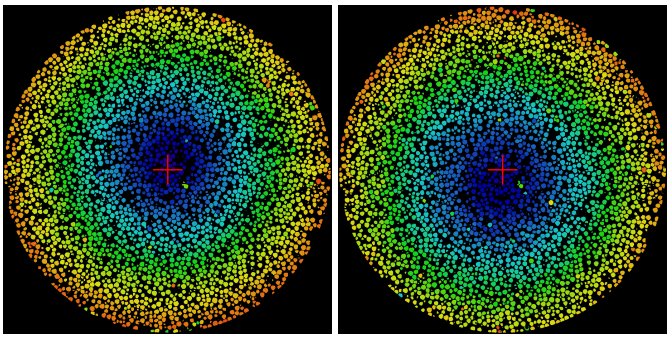

Figure 4: Slice of the binary image at two different points in time. Each particle is colored according to the distance it travels in the subsequent time step, blue indicates small and red indicates large values. In the first time step (left) the center of rotation is slightly above and in the second time step (right) it is below and left of the center of the sample. The image centers are marked with a red cross.

2.3.4. Estimating the axis of rotation

When analyzing the tracked particle data it becomes apparent that the empirical axis of rotation does not necessarily coincide with the central axis of the cylindrical sample (see Figure 4). The deviations can be caused by small inaccuracies in the alignment of the glass capillary and the upper and lower piston in the experiment, cf. Section 2.2.2, and lead to an overestimation of angular velocities on the one side and to an underestimation on the other side of the cylinder. In order to adjust for these effects, the axis of rotation is estimated from the data.

If rotation around a roughly vertical axis occurs, particles with the same height and horizontal distance from the axis of rotation will have approximately the same velocity. This means that the center of rotation at a given height can be estimated by fitting a circle to the particles at this height which have similar velocities. Note that the velocity of a particle is measured as the distance it travels per degree of shearing, i.e., it has the unit µm/°. For a grid of heights and velocities the corresponding particles are collected and a circle parallel to the xy-plane is fitted to their centers using weighted least squares, where the weight of each particle is determined by how closely it matches the velocity and z-coordinate of interest. More precisely, the weight of a particle p in the circle fitting for height z and velocity v is given by

$$w_p(z, v) = \exp\left(-\frac{(z - z_p)^2}{2h_z^2} - \frac{(v - v_p)^2}{2h_v^2}\right), \tag{4}$$

where z_p and v_p are the z-coordinate and velocity of p, and h_z and h_v are smoothing parameters. The center of rotation at height z is then determined by calculating the average of the circle centers fitted for height z, i.e., over all velocities in the grid. Note that the axis of rotation estimated in this way does not necessarily need to be a straight line but can be curved. In addition, the (curved) axis depends on the time step for which velocities have been computed, so it can change over time.

The smoothing parameters h_z and h_v control how many particles are relevant for each circle fitting. They should be large enough so that the circle fitting yields stable results, and small enough to allow the estimated circle centers to vary with height and velocity. In the present study they have been set to h_z = 11 µm and h_v = 0.66 µm/°. For these parameters, the resulting axis is a smooth but flexible 3D curve.

Note that no rotation occurs at the bottom of the sample. Here, all particles have a velocity close to zero and therefore approximately the same weight in the circle fitting. Due to the cylindrical shape of the domain, the estimated axis of rotation will automatically be dragged towards the center of the sample in these regions.

2.4. Simulations

2.4.1. Contact model

A soft particle DEM approach is utilized to simulate the system of interest, i.e., trajectories are calculated by numerically solving Newton's equations of motion. Particles interact via pairwise forces ($\vec{F}_{ij}$) and torques, which, in general, depend on their relative position ($\vec{r}_{ij} = \vec{r}_i - \vec{r}_j$), velocity, angular velocity, diameter (d_i, d_j) and the contact history to account for friction. The functional form of how forces and torques depend on the listed properties is generally referred to as the "contact model". It is convenient to distinguish between the normal part of the contact force, which describes the particles' response to a head-on impact as a function of the their overlap, $\xi = |\vec{r}_{ij}| - 1/2\,(d_i + d_j)$, and the tangential part, which, together with contact torques, complements the interaction on oblique impacts and accounts for friction.

Contact mechanics is a research field of continuous, intense study and today's literature offers a vast variety of sophisticated contact models (e.g. [30, 31, 32]), which are believed to provide an accurate interaction of micron-sized, spherical particles. However, this gain of accuracy is accompanied by an increasing complexity and many input parameters, which demand an elaborate experimental characterization [20]. Including such microscopic details in the model may not be beneficial for a deeper understanding of the bulk's behavior. Therefore, we employ a more phenomenological approach and intentionally keep the contact model and the parameter choice as simple as possible, exploring its predictive power as well as its limitations.

As a normal part for the contact model, we choose a damped Hertz model [33] and subtract, in accordance with DMT theory [34], a (positive) cohesion force (F_c) as a normal force

$$F_\mathrm{n}(\xi, \dot{\xi}) = \frac{4E_\mathrm{eff}\sqrt{r_\mathrm{eff}}}{3}\xi^{\frac{3}{2}} + \gamma_\mathrm{n}\sqrt{\xi}\dot{\xi} - F_c(r_\mathrm{eff}). \tag{5}$$

Here, $E_\mathrm{eff} = E/(2(1-\nu^2))$ is the effective elastic modulus, γ_n a viscous constant and $r_\mathrm{eff} = d_i d_j/(2(d_i + d_j))$ the reduced radius of the particles i and j. Consistently, a linear dependence of F_c on r_eff is employed, although we expect a minor influence due to the narrow particle size distribution.

The micromechanical description of the tangential forces (based on Cattaneo-Mindlin-Deresiewicz [35]) is reduced to the essence of friction [36], as is common practice in DEM simulations (see e.g. [37]). To implement Coulomb friction, together with rolling and torsional friction, we use the approach presented in [37]. Each contact mobilization mode (sliding,

rolling and twisting) is suppressed individually by using a linear spring-dashpot, until a threshold is exceeded. This threshold, as well as the resisting force (or torque) in case of mobilization, is proportional to $|F_\mathrm{n} + F_c|$. For simplicity, the same friction coefficients are used in the static and dynamic case.

2.4.2. Parameters and calibration

A proper choice of contact model parameters is essential to describe the material's flow behavior correctly. As already discussed above, this statement can only hold true within certain limitations, which will be explored as a secondary objective. Nevertheless, microscopically undetermined parameters can be utilized to calibrate a contact model, and they enable a correct description of the bulk's macro-scale behavior [25], e.g., stress response to applied strain.

The normal part of the contact model (Equation (5)) employs parameters which affect the elastic, viscous and adhesive behavior. Particle stiffness and adhesion force are measured experimentally (cf. Section 2.1), γ_n is undetermined a priori. In this study, the bulk's response to a quasi-static deformation is analyzed, hence, viscous parameters should have a negligible influence. For computational convenience, a high damping coefficient is used to optimize energy dissipation, well aware of the detachment effect [38]. In order to avoid overdamped dynamics, damping is coupled to the elastic modulus, i.e., we choose $\gamma_n = \sqrt{4/3\, E_\mathrm{eff} m_\mathrm{eff}}$, where m_eff is the reduced mass of the colliding particles. Parameters for the tangential part of the contact model are experimentally undetermined, leaving room for calibration. A typical choice for the tangential stiffness is $k_t = 2/7\, k_n$ [39], where k_n is $\frac{\partial}{\partial \xi} F_n^{(\mathrm{el})}$ with $F_n^{(\mathrm{el})}$ being the elastic part of Equation (5). Here we use $k_n = 4/3\, E_\mathrm{eff}\, x_{50,3}/2$, approximating the contact radius with the median particle radius and therefore overestimating the stiffness. Since the underlying friction model provides accurate results [36], the exact choice of k_t plays only a minor role [40]. All springs utilized for friction are damped, using a viscoelastic constant of $2\sqrt{k_t\, m_\mathrm{eff}}$. As twisting and sliding are closely related frictional modes, we set the torsion friction coefficient, $\mu_\mathrm{tor}/r_\mathrm{eff}$, equal to the Coulomb friction coefficient μ (overestimating friction effects [41]). As proposed in [30], we employ a load dependent rolling friction coefficient and set $\mu_\mathrm{rol} = \sqrt{2 r_\mathrm{eff} \xi}$. This choice of parameters leaves the Coulomb friction coefficient, μ, as a free parameter to calibrate the contact model.

The chosen particle size distribution is based on the experimental characterization by laser diffraction (cf. Section 2.1, Figure 1), using the following procedure: We model the distribution with a log-normal distribution and draw particle diameters according to the corresponding probability function. Only diameters between 25 µm and 50 µm are accepted, resulting in a slightly sharper cut-off at small particle sizes and an interquartile distance of $x_{75,3} - x_{25,3} \approx 5$ µm.

Calibration of the contact model is done by executing plane shear simulations under variation of μ at a fixed normal stress, $\sigma = 15$ kPa, and comparing the steady state macroscopic friction coefficient μ_macro to the experimental findings. These calibration simulations are done with $N = 10\,000$ particles, confining walls moving in shear direction and periodic boundary conditions in all other directions (see [21, 25] for details). The characteristic dependence $\mu_\mathrm{macro}(\mu)$ as found in many other studies (e.g. [5]) can be reproduced. Fitting an exponential saturating function as suggested in [42] results in $\mu \approx 0.58$.

2.4.3. Setup and preparation

The simulation setup mimics the experimental micro shear-tester explained in Section 2.2.2: A cylinder with diameter of 1.78 mm is used to confine the sample in horizontal direction, while two pistons (one movable, one fixed) close the simulation cell in vertical direction. Both pistons are structured similar to the experiment, i.e., with six vanes arranged in a star shape. The shear cell diameter is chosen slightly smaller than in the experiment in order to reduce the number of particles in the simulation. Wall-wall interaction can be turned off in simulations, hence the bottom piston, as well as the vanes, can in principle be extended to the outer capillary without a gap. As there is a small gap in the experiment (≈ 0.025 mm), we introduce a finite distance between the outer edge of the piston and the cylinder wall of ≈ 0.1 mm. This slight gap enlargement is required to avoid jamming of single particles between the piston and capillary since we neglect plastic deformation of particles. Particle-wall interaction is described by the visco-elastic part of the contact model (Equation (5)), using the same material parameters.

The preparation procedure includes the following steps: A random, porous particle configuration with volume fraction ≈ 0.2 is created. Potential overlaps are removed in a relaxation run that uses a viscous background friction. After relaxation, this omnipresent viscous term is removed and a normal load of 0.5 kPa is applied to the lower piston, compressing the material. Following compression, a constant angular velocity ω is added in order to shear the sample. To achieve a quasi-static deformation, we use the criterion $\omega \sqrt{\rho_\mathrm{s}\, x_{50,3}^2/\sigma} \approx 10^{-4}$, similar to [5].

3. Results

In order to analyze the shear induced structural heterogeneity of cohesive granular matter, we conducted a torsional shear experiment under constant normal load and implemented DEM simulations mimicking the experiment on the same scale (cf. Sections 2.2 and 2.4). As the ratio of cohesion force to normal stress is $\eta = F_c/(\sigma x_{50,3}^2) \approx 0.2$, only a minor influence of cohesion is expected [16]. Starting from a consolidated configuration, a total shear strain of $\omega t \approx 39.5°$ is analyzed and compared. In Section 3.1 we compare the spatially-resolved number density of particle centers in experiment and simulation. Different methods for the detection and analysis of shear bands are presented in Sections 3.2 and 3.3, based on tomographic images and particle tracking, respectively. Finally, the shear band location and shape are compared in experiment and simulation.

3.1. Segmentation and structural analysis

To extract particle positions from the experimental configuration, tomographic data was segmented as explained in Section 2.3.2. Particle positions and radii have been determined by

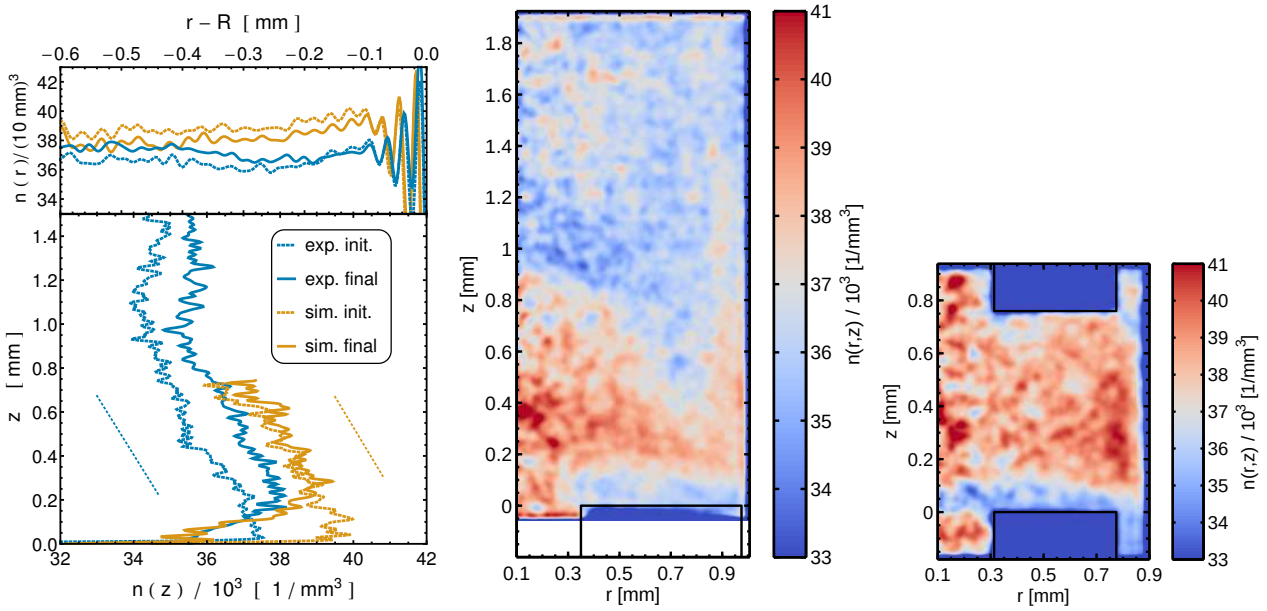

Figure 5: Axial and radial density profiles (w = 8.8 µm) of the initial and the final configuration (left). 2D density profiles (w = 14.9 µm) of the experimental (center) and numerical (right) final configurations. In all plots $z = 0$ marks the upper edge of the vanes on the bottom piston.

calculating the center of mass and the volume-equivalent radius (i.e., the radius of a ball with the same volume) of the voxel representation of each particle. Particles with a diameter smaller than 13.2 µm or larger than 53.0 µm have been excluded from the analysis. Very small particles cannot be segmented reliably, while unrealistically large particles may occur due to bright, star-like artifacts, which seem to be caused by single particles of a different material present in the sample. Note that the excluded particles correspond to less than 0.1 % of the whole particle volume at each point in time.

The distribution of particle diameters extracted from the segmented image data is unimodal and slightly skewed to the left with a median of $x_{50,3}$ = 30.7 µm and an interquartile distance of $x_{75,3} - x_{25,3}$ = 3.7 µm. The size distribution has also been measured using laser diffraction (cf. Section 2.1), where a very similar median of $x_{50,3}$ = 29.8 µm was observed. The interquartile distance obtained from laser diffraction is $x_{75,3} - x_{25,3}$ = 11.0 µm, i.e., considerably larger than the value based on the image data. This is most likely due to the back calculation algorithm used for laser diffraction measurements, which is known to overestimate the width of extremely narrow particle size distributions [43]. Importantly, the particle size distribution estimated based on the image data is almost identical for all XMT measurements, indicating consistent segmentation results.

Based on the centers of the segmented particles, we compare the number density $n(r, z)$, i.e., the number of particles per cubic millimeter, as a function of height (z) and distance to the central axis of the cylindrical sample chamber (r). Furthermore, rotational invariance is assumed, hence all data is averaged over φ. To obtain continuous fields, we coarse-grain the data with a Gaussian kernel (with standard deviation w).

Axial and radial density profiles of the initial and final configurations are shown in Figure 5, together with 2D snapshots of the final configurations. Experimental and numerical results are aligned so that the outer cylinder walls coincide. Segmentation of the image data reveals that the number of particles in experiment exceeds the simulation by roughly a factor of 2.5, resulting in a greater filling height. Hence, only a comparable region 0 mm $\leq z \leq$ 0.7 mm was considered for the radial density profile and only the portion between the pistons is displayed in the axial density profile ($z = 0$ marks the upper edge of the lower piston). While densities in experiment and simulation are of the same order of magnitude, the densities in the simulation are systematically higher. A coarse-graining length of w = 8.8 µm nicely reveals wall-induced layering, as shown in all radial density profiles ($r - R > -0.1$ mm, recall that R is the shear cell radius) for both experiment and simulation (Figure 5 (left)). This signature of granular microstructure is known from shear experiments [8]. However, the increasing density in the wall's vicinity, which can be seen in the radial and in the 2D density profiles in Figure 5, suggests an even larger wall influence of roughly 1/4 mm $\approx 8\ x_{50,3}$, which is not surprising, as long-range wall perturbations can be present with quasi-static deformations [44]. Besides these dense zones close to the wall, a slight gradient in radial direction can be detected in the bulk as well. While the density increases with r in the numerical data, the shear cell's center is more densely packed in the experiment. This deviation can already be spotted in the initial configuration and may therefore be a relict of the different preparation procedure, as discussed later. Judged by the radial density profiles, shearing leads to dilation in simulations, whereas the experimental packing compacts/densifies during shear. This misconception can be cleared up by the axial density distribution. Comparing the initial and final configurations, a dilation ($0 \leq z \leq 0.2$ mm) as well as a compaction

zone ($z > 0.2$ mm) can be identified in both simulation and experiment. Densification is much more pronounced in the experiment and the ratio of compacting to dilating volume part is close to unity in simulation leading to the illusion of dilation. Despite these quantitative differences, the axial density profiles are in qualitative agreement. Even quantitative agreement is achieved when looking at the unique/specific features of the axial density profiles: The omnipresent density gradient ($z < 1$ mm) in z-direction, which can be quantified by a linear fit (indicated in the plot), just differs by less than 5 %. Shearing leads to a decrease of the gradient's absolute value from approximately $4.4 \cdot 10^3$ 1/mm^4 to $3.5 \cdot 10^3$ 1/mm^4. This gradient is probably caused by wall friction and can be interpreted as a consequence of the Janssen effect [45], which will be discussed later (Sections 4.1). Another unique feature of the final axial density profile is the dilating zone, where the experimental and the numerical data collapse, suggesting a shear localization close to the lower piston with the *same* critical density. Further analysis of the shear localization is part of Section 3.2 and 3.3.

The 2D number density plots (Figure 5; center and right) emphasize the spatial inhomogeneity of the density distribution, which was already revealed by the 1D profiles. As seen, e.g., in the experimental data, from bottom to top, a dilation zone is located directly above the lower piston, followed by a more densely packed zone above which a homogeneous zone is located. A higher number density close to the wall can be observed as well. Ignoring the inhomogeneity induced by the capillary wall, the 2D density plots suggest a cone like densification zone on top of the lower piston. This feature is not prominent in the simulation data, where the dense region close to the outer wall is more pronounced.

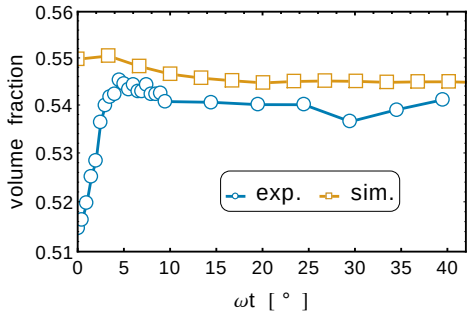

Figure 6: Comparison of the mean volume fraction over time.

By estimating the total particle volume based on the binary images and normalizing with the volume of the sample chamber, we are also capable of tracking the experimental solids volume fraction over time and of comparing the results with the simulation data, shown in Figure 6. As already observed in the local number density, the shear induced compaction is more pronounced in the experiment ($\omega t \leq 5°$). This difference is probably caused by the dense initial configuration in the simulation. The initial densification is followed by a dilation in experiment and simulation until a steady state volume fraction is reached at a shear strain of $\omega t \approx 10°$ in experiment and $\omega t \approx 20°$ in the simulation run. We notice, however, that the fluctuations in the experimental data do not support a final statement on when exactly the steady state is reached. The analysis on shear localization will lead to further insight.

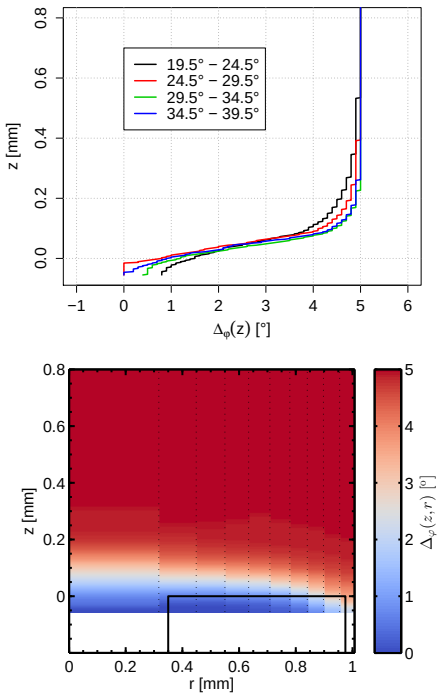

Figure 7: Image-based local shear deformation in 1D and 2D in the steady state of the experiment. The 1D case (top) shows the shear deformation as a function of the height in the sample with almost congruent states. The 2D deformation, which is shown for the last time step as an example (bottom), reveals that the shear band geometry is curved close to the wall.

3.2. *Image-based local shear deformation*

The image-based local shear deformation was determined in 1D and 2D for the experimental data as described in Section 2.3.1, based on the tomographic grayscale image stacks. Results for the final four time steps are shown in Figure 7. We obtain an angle of local deformation as a function of the height in the sample (z) in 1D, and as a function of the height (z) *and* the distance from the central axis of the cylinder (r) in 2D. Note that based on the image data we only obtain a coarse radial resolution: The number of radial coordinates for which the local shear deformation is evaluated corresponds to the number of rings rotated independently (cf. Section 2.3.1). This number cannot be very large, because we need a certain number of voxels on each ring in order to get reliable results.

Shear strain localizes close to the lower piston, as already suggested by the density profiles. The 1D deformation shows that the extension of the shear band still varies after $\omega t \approx 10°$, although the volume fraction already remains constant after this point (see Figure 6). Starting at $\omega t \approx 25°$ no significant changes in the deformation behavior can be observed. In 2D we obtain more details about the geometric shape of the shear band. In addition to its location and width, the 2D deformation reveals that the shear band is curved downwards where the vanes on

the lower piston meet the cylinder wall. This means that directly above the lower piston particles close to the wall have a higher angular velocity than particles in the center of the sample. Again, the effect can be explained by the influence of the outer rotating wall because outer particles are more easily dragged along than particles in the center of the sample. We observe a vertical extension of the shear band of up to 250 µm after $\omega t \approx 25°$, which corresponds to approximately 8 median particle diameters. This agrees well with data from literature, where ratios between 7 and 18 have been found [10, 13, 26, 46]. The 2D deformation additionally suggests that the shear band is broader towards the center of the sample than close to the outer wall.

The 1D image-based local shear deformation can also be used to measure the rotation of the upper and lower piston (see Section 2.3.1). In principle, the movement of the pistons should be known from the setup of the experiment: the upper piston should rotate in steps of 0.5° and later 5°, while the lower piston should be held perfectly still. However, we observe that the actual movement of the pistons deviates from this ideal. The mean absolute difference between the actual and target angle of rotation is 0.02° for the upper and 0.19° for the lower piston, respectively. Taking into account both, the mean absolute difference between the actual and target angle of shear is 0.20°.

This imperfection in the rotational movement is likely caused by the compensation unit, which is supposed to keep the contactless mounted lower piston in place while tracking shear stress. However, interlocking of particles between piston and wall may counteract this mechanism, dragging the lower piston partially during shear deformation and resulting in implausible high peaks in the shear stress. A solution for this problem can be obtained by decreasing the piston diameter (and thus increasing the gap) to reduce the effects of interlocking. However, this is accompanied by the more disadvantageous effect of loosing sample material, which may be pushed through the gap and out of the sample chamber during shear. Moreover, we can only control the rotation of the upper piston and hence of the glass capillary in this shear-tester setup. Unfortunately, it is not possible to observe the rotation of the lower piston in the range of $\approx 0.01°$ during shear deformation to achieve the desired relative rotation.

3.3. Tracking and shear bands

Particle tracking allows for an even more detailed analysis of strain localization in the experiment compared to the image-based analysis of Section 3.2.

Particle tracks were computed for all steps of shearing starting at $\omega t = 3.5°$ using the methods described in Section 2.3.3. Before this point we observe a considerable decrease in the distance between upper and lower piston, from 2.12 mm to 1.93 mm, which leads to considerably high vertical displacements of particles in the upper part of the cylinder. This shear-induced densification, which is even spatially inhomogeneous, renders the identification of reliable tracks in the first time steps impossible. After $\omega t = 3.5°$ we obtained very good tracking results. The tracking efficiency (measured as the number of particles assigned to valid tracks divided by the total number of particles) is larger than 97 % in each step of 5°, and even larger than 99.5 % in each step with an angle increment of 0.5°.

On the basis of particle tracks, it is possible to calculate velocities of single particles in the experiment and compare them to the simulation. For reasons of comparability, all particle velocities are described as angular velocities with respect to the axis of rotation (cf. Section 2.3.4), and normalized to the interval [0, 1] using the movements of upper and lower piston, which are estimated as described in Section 2.3.1. All movements are described relative to the upper piston and wall.

We compare the 2D profiles of average normalized angular velocity, $v_{\tilde{\varphi}}(\tilde{r}, z)$, as a function of height (z) and (horizontal) distance to the axis of rotation ($\tilde{r}$), where the average is in $\tilde{\varphi}$-direction and $(\tilde{r}, \tilde{\varphi}, z)$ denote cylindrical coordinates with respect to the axis of rotation. Note that in case of the experiment, the axis of rotation has been *estimated from the data* as described in Section 2.3.4 and rotational velocities are calculated with respect to this estimated axis. In the simulation, however, we did not observe severe deviations of the axis of rotation from the central axis of the cylinder, so the two are considered equivalent. This change of the coordinate system is necessary because the dynamics in the sample clearly depend on the distance from the axis of rotation rather than the distance from the central axis of the cylinder. Without adjusting the cylindrical coordinates, the experimental particle velocities would not be independent of φ and averaging in azimuthal direction would not be feasible. For coarse-graining we used the same bandwidth as for the 2D density profiles in Section 3.1, $w = 14.9$ µm.

In order to compare the shear bands visible in experiment and simulation quantitatively, we fitted a parametric function to the velocity profiles. For a fixed radial distance, $\tilde{r}$, the velocity profile is described well by the function

$$v_{\tilde{\varphi}}(z) = \frac{1}{2} - \frac{1}{2}\ \mathrm{erf}\left(\frac{z - z_{sb}}{w_{sb}}\right), \tag{6}$$

where erf denotes the error function, and z_{sb} and w_{sb} are the fitted parameters describing the local height and (semi) width of the shear band, respectively. This function is attractive because of its simplicity with only two parameters and has also been used in [9] to describe symmetric shear zones. Discretizing $\tilde{r}$ with a bin size of 0.03 mm and fitting this function to the z-coordinates and (normalized) velocities of the particles in each bin, we obtain estimates of $z_{sb} = z_{sb}(\tilde{r})$ and $w_{sb} = w_{sb}(\tilde{r})$ as functions of the radial distance $\tilde{r}$, leading to a $\tilde{r}$-dependent velocity profile $v_{\tilde{\varphi}}(z) = v_{\tilde{\varphi}}(\tilde{r}, z)$. Here, we define the shear band as the interval $z_{sb} \pm w_{sb}$, which covers approximately the central 84 % of the velocity range in the data. Of course, any other reasonably large percentage could be chosen to separate shear band and homogeneous zones in principle. Since the main purpose of the fit is to quantitatively compare experiment and simulation, we stick to this simple choice.

An example of actual and fitted velocity profiles in the simulation as well as the time-averaged velocity profile obtained for the experimental data after $\omega t \approx 10°$ is reached are shown in the upper part of Figure 8. The fitted shear band is indicated as

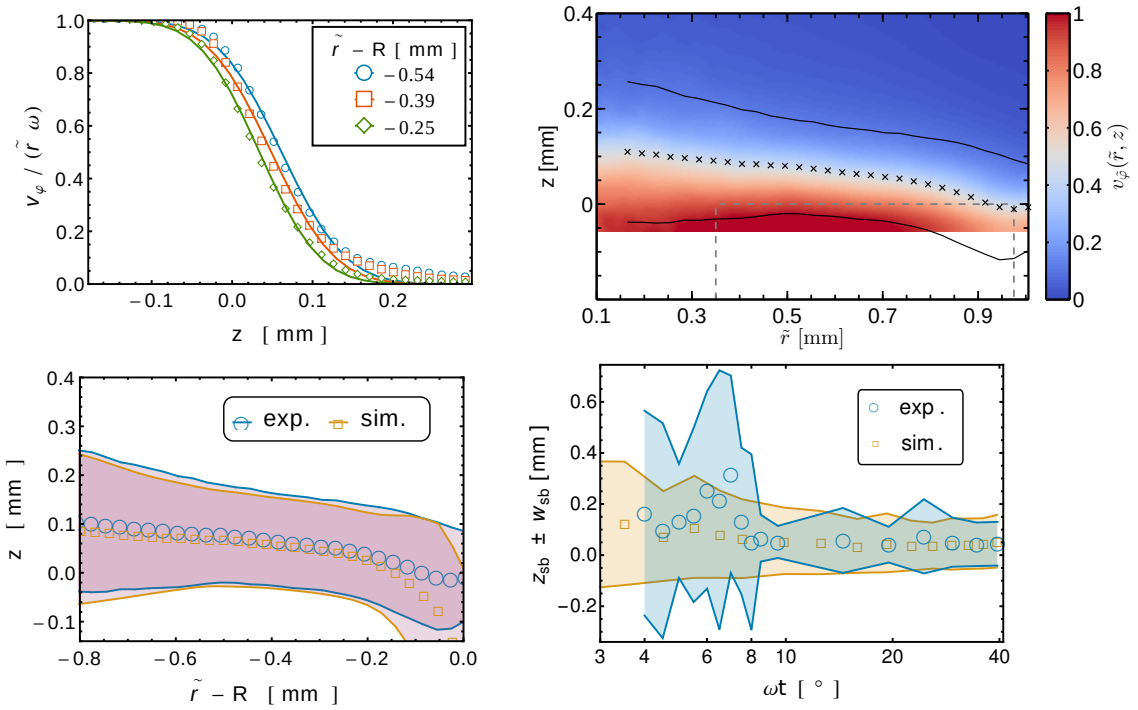

Figure 8: Example of actual and fitted velocity profiles in the simulation for one snapshot and different distances from the axis of rotation (top left), experimental 2D velocity profile in the steady state with the fitted shear band indicated in black (top right), comparison of the fitted shear bands after reaching the steady state in experiment and simulation (bottom left), and development of the fitted shear band width and location in simulation and experiment over time, averaged over $\tilde{r}$ (bottom right). The shear bands are indicated as $z_{sb} \pm w_{sb}$.

$z_{sb} \pm w_{sb}$ in the graph on the right-hand side. The graphs show a very good agreement of the fitted profiles with simulated and experimental data, respectively. The bottom left part of Figure 8 shows a direct comparison of the fitting results for simulation and experiment, where the alignment is chosen such that the outer cylinder walls coincide. The experimental and simulated shear bands are in almost perfect agreement. In both cases the shear band is close to the lower piston, on average its center is located at $z = 0.12$ mm. The shear band width is also very comparable, it is $2w_{sb} = 0.23$ mm on average, which corresponds to roughly 8 median particle diameters. Both shear bands are slightly curved downwards where they come close to the outer wall of the cylinder. While they coincide almost perfectly for $r - R \leq 0.2$ mm, the curvature close to the wall is stronger in the simulation, which can be explained by the larger gap between piston and wall (cf. Section 2.4.3).

The bottom right part of Figure 8 shows the development of z_{sb} and w_{sb} in experiment and simulation over time, averaged over $\tilde{r}$. It seems that a steady state is reached at $\omega t \approx 10°$ in the experiment and at $\omega t \approx 20°$ in the simulation, as already indicated by the solids volume fraction shown in Figure 6. Before $\omega t \approx 10°$ the experimental shear band width and height are (on average) larger, and both values fluctuate much more strongly. The shear band rises from $z_{sb} \approx 0.15$ mm to $z_{sb} \approx 0.37$ mm in this period and drops back to its lower position at a shear strain of $\omega t \approx 9°$. However, even after $\omega t \approx 10°$ the shear band width fluctuates perceptibly, w_{sb} takes values between 0.08 and 0.16 mm here. Smaller fluctuations have to be expected since we consider (and implicitly average over) much larger time intervals in each step here. There seems to be a second drop in the variability of z_{sb} and w_{sb} at $\omega t \approx 25°$. Whether this is a coincidence or the steady state is actually only reached in the last three steps of the experiment is unclear and cannot be judged based on the present data. Therefore, we assume that the steady state is reached at $\omega t \approx 10°$ in our analysis. In the simulation the initial shear band width and location are also higher than in the steady state, but the difference is smaller and the transition much smoother than in the experiment. This might either be due to the difference in the initial configurations (cf. Section 3.1) or due to stopping the process of shearing for XMT measurements in the experiment. As the experiment is conducted quasi-statically, no influence of inertia is expected. However, the entire shear cell has to be slowly rotated in the course of an XMT measurement, which might slightly alter particle positions and perturb the smooth transition into the steady state.

4. Discussion

4.1. Segmentation and structural analysis

Analysis of the static configurations revealed a systematically higher number density in the simulation data. The relative deviation of just 2.5 % is probably due to a very narrow particle size distribution in reality as determined based on the XMT measurements. Due to the back calculation algorithm of the laser diffraction device, a wider distribution was measured. Segmentation underlines this reasoning as the interquartile distance is indeed slightly larger in the simulation (5 µm

compared to 3.7 μm). However, other possible reasons why the packing fraction is overestimated in the simulation can be identified: While either a higher F_c [16], or a higher rolling friction coefficient [18] can lead to a decrease in volume fraction, an additive contribution of both effects is unlikely (e.g., dust or surface roughness in general would increase contact friction while decreasing the contact area and therefore van-der-Waals forces [20]). Since the adhesion force was measured experimentally, rolling friction might simply be underestimated by theory (cf. Section 2.4.2 and [26, 30]).

However, the mm-sized shear cell suggests also a great wall influence. Indeed, a more drastic influence should be expected in the simulations since the shear cell radius is roughly 0.1 mm smaller than in the experiment. Assuming a densification zone close to the wall with equal extent ($\approx$ 0.25 mm) and density, the increase in the number density due to a smaller shear cell radius can be approximated and should amount to about 1 %, accounting for half of the deviation in principle. However, the density in the wall's vicinity also differs, as the radial density profile revealed (Figure 5).

The simulation shows a more pronounced densification zone at the wall, while an almost cone-like densification zone is present in the center of the experimental shear cell. Because wall friction can have a drastic impact on the transfer of shear strain [47], the deviation might be caused by a combination of the approximated particle-wall interaction in the simulation (especially friction) and the different preparation procedure. During preparation in simulation, the lower piston is raised slowly by almost 2.5 mm, compacting the initial random packing (volume fraction ≤ 0.2) to the desired stress. This process already contains a shear strain at the capillary wall, i.e., wall friction leads to a continuous excitation in the outer region during compaction, which might induce a tapping like densification [7, 48]. As the relative motion of capillary and lower stamp is present in the experiment as well, the cone-like densification zone seems puzzling. Here, however, the preparation process is different, namely a gravitation driven deposition. The first portion of dumped particles piles onto the structured bottom piston (e.g. vanes arranged in a star shape), which quite likely dictates the densification zone's shape. In addition, the resulting configuration is more dense, requires less strain for compression and is therefore exposed to less excitation. Of course this interpretation needs further investigation. Given all these possible influences, a deviation in density of a few percent (volume fraction only 0.7 %) is more than satisfying.

Even better agreement is found in the axial density distribution. Although neither the exact particle-wall friction, nor adhesion is known, the same density gradient in z-direction is observed in both experiment and simulation. This gradient is caused by wall friction, demonstrating the stress-flux between piston and capillary. As the characteristic length scale in the Janssen effect grows with the ratio of cylinder radius and friction coefficient, we have to assume that both approximations cancel out, resulting in this quantitative agreement.

With respect to the different number densities in the compaction zone, it seems like a coincidence that the experimental and numerical curves collapse in the dilation zone (axial number density in Figure 5). A more optimistic interpretation would imply the *same* critical number density, since the dilation zone coincides with the shear band. While density inhomogeneity due to preparation remains in the resting part of the bulk, the active shear zone is history independent. The minor differences in particle size distribution seem not to affect this result.

4.2. Tracking and shear bands

In Sections 3.2 and 3.3 we presented the results of different methods to analyze shear bands in the experiment. Though they are in good agreement in principle, the methods vary in computational efficiency, flexibility and the level of detail of the information they provide. The 1D image-based local shear deformation is relatively fast to compute and provides a good first overview over the deformation as a function of the height in the sample. An extension of this method is the 2D image-based local shear deformation. Here, each image slice is not rotated as a whole — instead, the disk-shaped cross section of the cylinder is subdivided into disjoint rings, which are rotated independently (see Section 2.3.1). This extension is more computationally expensive (depending on the number of rings used), but in return provides 2D information: the local angle of shear deformation as a function of height *and* radial coordinate in the sample. In particular, it reveals that the shear band in our data is slightly curved and not exactly parallel to the xy-plane. We believe that the curved shape of the shear band is predominantly provoked by the influence of the outer glass wall. Such effects are concealed by the 1D deformation, which is similar to an average over r. If the shear band properties depend strongly on the radial coordinate, the 1D information might even be misleading. For example, a shear band which is actually narrow and strongly curved (which might, e.g., be caused by a strong sample heterogeneity) would seem like a wide shear band in the 1D deformation. In our case the shear band is only slightly curved and we obtain similar shear band widths with both methods. On that account the observed shear band width in our experiment agrees well with data in literature for noncohesive granular matter. With the ratio $F_c/(\sigma x_{50,3}^2) \approx 0.2$, this is expected [49].

The results presented in Section 3.3 were computed based on a particle tracking. Obtaining this particle tracking requires significant additional effort during the experiment as well as from a computational and analytic perspective. First, the XMT measurements are time consuming and a good temporal resolution is needed. Although we present a method to track the particles even in steps with an angle increment of 5°, much smaller angle increments are needed at least for part of the experiment to validate the method (see Section 2.3.3). Furthermore, the tracking itself requires a preceding segmentation of good quality and the 2D image-based local shear deformation discussed in the previous paragraph. In return, it provides information on the motion of single particles in the experiment, which is the most accurate basis for a shear band analysis. It is much more precise than the image-based method and revealed, for example, that the axis of rotation varies in the experiment. Such effects cannot be captured and accounted for by the image-based local shear deformation. Moreover, particle tracking bridges the gap between experimental data and discrete element simulations and makes

the two comparable. It enables the estimation of continuous velocity fields and a parametric fit of the shear band parameters in a very fine radial resolution. Our comparison to simulations shows a very good agreement of experimental and simulated shear band shape and location. Though not performed in this study, the particle tracking additionally allows for the comparison of single particle trajectories and their properties, which will be subject of future work.

The Gaussian function given in Equation (6), which we used for fitting the shear bands, proved to provide very good fits for shear bands in a modified Couette shear cell [9]. These shear bands develop distant from a wall, resulting in a symmetric shape. When shear bands develop close to a wall, such perfectly symmetric shapes are not typical. For example, a mixture of a Gaussian and an exponential component in the velocity profile was observed in a study of shear bands localized close to the side wall in a similar shear cell geometry [7, 8]. The exponential decay was attributed to slippage between layers of the monodisperse particles used in [8]. In our data, the velocity profiles appeared approximately symmetric, thus we consider only the purely Gaussian fitting function. If an exponential component is present in our data, it is very small. This is plausible because we cannot have layers of particles at the bottom of the cylinder due to the structured pistons. A wider particle size distribution might be another reason why we do not observe layers of particles slipping over each other at the bottom of the shear cell in this study.

5. Conclusion and outlook

In this study we demonstrated that an experiment and a DEM simulation of particles under torsional shear can be realized on the same scale. We used spherical particles made of borosilicate glass. Even with a comparatively simple contact model, which does not include plastic deformations, we obtained a very good agreement of the dynamics in simulation and experiment. This direct comparison suggests, however, that effects caused by the initial structure of the particle system do not vanish completely during the observed strain deformation and, therefore, caution has to be taken at preparation stage.

Using the micro shear-tester implemented in an XMT device we can image the evolution of the sample during the experiment in a series of high-resolution 3D images. Particle positions and radii can be extracted consistently from the image data and have been used to compute spatially resolved density profiles of the particle centers, which were in good qualitative agreement for experiment and simulation. We presented methods to assess the local shear deformation in the sample based directly on the image data as a function of height and radial coordinate in the cylindrical sample chamber. Furthermore, we demonstrated how this information can be used to identify tracks of single particles even when a large angle increment of up to 5° is used for shearing between XMT measurements. This even more detailed data on the movements of particles can be used to directly compare the dynamics in experiment and simulation. Although the slightly different preparation and the unsteady experimental procedure complicate a direct comparison of the temporal evolution, we obtained an extremely good agreement of the shear bands in the steady state. The shear band developed close to the lower piston and is slightly curved downwards at the outer wall of the cylinder. Using a Gaussian function to fit the profile of rotational velocities for a series of radial coordinates, we obtained quantitative agreement of the shear band width and location in experiment and simulation over almost the full radius of the shear cell.

This paper presents a toolbox of methods to analyze a shear experiment based on tomographic image data. Naturally, the methods can also be used to compare multiple experiments with varied parameters or multiple types of particles. Further work has to be done to address some more questions regarding particle trajectories in order to resolve single particle profiles during shear. Another raising question deals with the effect of the sample preparation process on the initial packing behavior which is not worked on in detail in the current study. Moreover, an extension of the considered parameters is possible. Here, a shear stress logging during deformation and an investigation of the effect of larger stress levels on the packing and deformation behavior is desirable. Additional scenarios should be addressed to describe structural and dynamic effects in fine granular matter. These include variation of particle parameters such as particle surface forces as a modification of particle cohesion, investigation of particle shapes far away from ideal spherical shape, e.g., rods and irregular shaped glass particles, or a variation of particle size distribution and its effect on mesoscopic deformation.

Acknowledgments

This work was funded and prepared within the priority program SPP 1486 by the Deutsche Forschungsgemeinschaft (DFG).

References

[1] M. A. Polizzi, J. Franchville, J. L. Hilden, Assessment and predictive modeling of pharmaceutical powder flow behavior in small-scale hoppers, Powder Technol. 294 (2016) 30–42.

[2] M. C. Garcia, H. J. Feise, S. Strege, A. Kwade, Segregation in heaps and silos: Comparison between experiment, simulation and continuum model, Powder Technol. (in print), doi: http://dx.doi.org/10.1016/j.powtec.2015.09.036.

[3] K. Grudzien, M. Niedostatkiewicz, J. Adrien, E. Maire, L. Babout, Analysis of the bulk solid flow during gravitational silo emptying using X-ray and ECT tomography, Powder Technol. 224 (2012) 196–208.

[4] H. M. Jaeger, S. R. Nagel, Physics of the granular state, Science 255 (1992) 1523–1531.

[5] F. Da Cruz, S. Emam, M. Prochnow, J.-N. Roux, F. Chevoir, Rheophysics of dense granular materials: discrete simulation of plane shear flows, Phys. Rev. E 72 (2005) 021309.

[6] K. Kamrin, G. Koval, Nonlocal constitutive relation for steady granular flow, Phys. Rev. Lett. 108 (2012) 178301.

[7] A. Ries, L. Brendel, D. E. Wolf, Shearrate diffusion and constitutive relations during transients in simple shear, Comput. Part. Mech. (in print), doi: http://dx.doi.org/10.1007/s40571-015-0058-3.

[8] D. M. Mueth, G. F. Debregeas, G. S. Karczmar, P. J. Eng, S. R. Nagel, H. M. Jaeger, Signatures of granular microstructure in dense shear flows, Nature 406 (2000) 385–389.

[9] D. Fenistein, J. W. van de Meent, M. van Hecke, Universal and wide shear zones in granular bulk flow, Phys. Rev. Lett. 92 (2004) 094301.

[10] S. Nemat-Nasser, N. Okada, Radiographic and microscopic observation of shear bands in granular materials, Géotechnique 51 (2001) 753–765.
[11] R. Moosavi, M. R. Shaebani, M. Maleki, J. Török, D. E. Wolf, W. Losert, Coexistence and transition between shear zones in slow granular flows, Phys. Rev. Lett. 111 (2013) 148301.
[12] F. Varnik, L. Bocquet, J.-L. Barrat, L. Berthier, Shear localization in a model glass, Phys. Rev. Lett. 90 (2003) 095702.
[13] C. M. Gourlay, A. K. Dahle, Dilatant shear bands in solidifying metals, Nature 445 (2007) 70–73.
[14] C. Thornton, L. Zhang, On the evolution of stress and microstructure during general 3D deviatoric straining of granular media, Géotechnique 60 (2010) 333–341.
[15] F. A. Gilabert, J.-N. Roux, A. Castellanos, Computer simulation of model cohesive powders: plastic consolidation, structural changes, and elasticity under isotropic loads, Phys. Rev. E 78 (2008) 031305.
[16] P. G. Rognon, J.-N. Roux, M. Naaim, F. Chevoir, Dense flows of cohesive granular materials, J. Fluid Mech. 596 (2008) 21–47.
[17] S. Luding, Micro-macro transition for anisotropic, frictional granular packings, Int. J. Solids Struct. 41 (2004) 5821–5836.
[18] D. Kadau, G. Bartels, L. Brendel, D. E. Wolf, Pore stabilization in cohesive granular systems, Phase Transit. 76 (2003) 315–331.
[19] T. Pöschel, C. Salueña, T. Schwager, Can we scale granular systems?, in: Powders and Grains 2001, CRC Press, Boca Raton, 2001, pp. 439–442.
[20] R. Fuchs, T. Weinhart, J. Meyer, H. Zhuang, T. Staedler, X. Jiang, S. Luding, Rolling, sliding and torsion of micron-sized silica particles: experimental, numerical and theoretical analysis, Granul. Matter 16 (2014) 281–297.
[21] S. Strege, A. Weuster, H. Zetzener, L. Brendel, A. Kwade, D. E. Wolf, Approach to structural anisotropy in compacted cohesive powder, Granul. Matter 16 (2014) 401–409.
[22] I. Vlahinić, E. Andò, G. Viggiani, J. E. Andrade, Towards a more accurate characterization of granular media: extracting quantitative descriptors from tomographic images, Granul. Matter 16 (2013) 9–21.
[23] J. Wenzl, R. Seto, M. Roth, H.-J. Butt, G. K. Auernhammer, Measurement of rotation of individual spherical particles in cohesive granulates, Granul. Matter 15 (2013) 391–400.
[24] G. Viggiani, N. Lenoir, P. Besuelle, M. Di Michiel, S. Marello, J. Desrues, M. Kretzschmer, X-ray microtomography for studying localized deformation in fine-grained geomaterials under triaxial compression, C. R. Mécanique 332 (2004) 819–826.
[25] A. Weuster, S. Strege, L. Brendel, H. Zetzener, D. Wolf, A. Kwade, Shear flow of cohesive powders with contact crystallization: experiment, model and calibration, Granul. Matter 17 (2015) 271–286.
[26] S. Strege, Röntgenmikrotomographische Analyse der Verdichtung und Scherung feiner und kohäsiver Pulver, Ph.D. thesis, TU Braunschweig (2014).
[27] E. R. Doughtery (Ed.), Mathematical Morphology in Image Processing, Marcel Dekker Inc., New York, 1993.
[28] T. W. Ridler, C. S, Picture thresholding using an iterative selection method, IEEE T. Syst. Man Cyb. 8 (1978) 630–632.
[29] J. C. Crocker, D. G. Grier, Methods of digital video microscopy for colloidal studies, J. Colloid Interf. Sci. 179 (1996) 298–310.
[30] J. Tomas, Adhesion of ultrafine particles - a micromechanical approach, Chem. Eng. Sci. 62 (2007) 1997–2010.
[31] C. Thornton, K. K. Yin, Impact of elastic spheres with and without adhesion, Powder Technol. 65 (1991) 153–166.
[32] C. Thornton, Z. M. Ning, A theoretical model for the stick/bounce behaviour of adhesive, elastic-plastic spheres, Powder Technol. 99 (1998) 154–162.
[33] N. V. Brilliantov, F. Spahn, J. M. Hertzsch, T. Pöschel, Model for collisions in granular gases, Phys. Rev. E 53 (1996) 5382–5392.
[34] B. V. Derjaguin, V. M. Muller, Y. P. Toporov, Effect of contact deformations on adhesion of particles, J. Colloid Interf. Sci. 53 (1975) 314–326.
[35] K. L. Johnson, Contact Mechanics, Cambridge University Press, Cambridge, 1987.
[36] J. Schäfer, S. Dippel, D. E. Wolf, Force schemes in simulations of granular materials, J. Phys. I 6 (1996) 5–20.
[37] S. Luding, Cohesive, frictional powders: contact models for tension, Granul. Matter 10 (2008) 235–246.
[38] S. Luding, E. Clément, A. Blumen, J. Rajchenbach, J. Duran, Anomalous energy dissipation in molecular-dynamics simulations of grains: the "detachment" effect, Phys. Rev. E 50 (1994) 4113–4122.
[39] L. E. Silbert, D. Ertaş, G. S. Grest, T. C. Halsey, D. Levine, S. J. Plimpton, Granular flow down an inclined plane: Bagnold scaling and rheology, Phys. Rev. E 64 (2001) 051302.
[40] C. Campbell, Granular shear flows at the elastic limit, J. Fluid Mech. 465 (2002) 261–291.
[41] S. R. Dahmen, Z. Farkas, H. Hinrichsen, D. E. Wolf, Macroscopic diagnostics of microscopic friction phenomena, Phys. Rev. E 71 (2005) 066602.
[42] A. Taboada, N. Estrada, F. Radjaï, Additive decomposition of shear strength in cohesive granular media from grain-scale interactions, Phys. Rev. Lett. 97 (2006) 098302.
[43] R. Xu, Particle Characterization: Light Scattering Methods, Kluwer Academic Publishers, New York, 2002.
[44] P. G. Rognon, T. Miller, B. Metzger, I. Einav, Long-range wall perturbations in dense granular flows, J. Fluid Mech. 764 (2015) 171–192.
[45] H. A. Janssen, Versuche über Getreidedruck in Silozellen, Z. Ver. dtsch. Ing. 39 (1895) 1045–1049.
[46] P. Guo, Critical length of force chains and shear band thickness in dense granular materials, Acta Geotech. 7 (2012) 41–55.
[47] Z. Shojaaee, L. Brendel, J. Török, D. E. Wolf, Shear flow of dense granular materials near smooth walls. ii. block formation and suppression of slip by rolling friction, Phys. Rev. E 86 (2012) 011302.
[48] J. B. Knight, C. G. Fandrich, C. N. Lau, H. M. Jaeger, S. R. Nagel, Density relaxation in a vibrated granular material, Phys. Rev. E 51 (1995) 3957–3963.
[49] A. Singh, V. Magnanimo, K. Saitoh, S. Luding, Effect of cohesion on shear banding in quasistatic granular materials, Phys. Rev. E 90 (2014) 022202.